Photonics enhances sensors for food monitoring: part 1

Meulebroeck, Wendy; Thienpont, Hugo; Ottevaere, Heidi

Published in:
IEEE Instrumentation & Measurement Magazine

Publication date:
2016

Photonics Enhanced Sensors for Food Monitoring: Part 1

Wendy Meulebroeck, Hugo Thienpont, and Heidi Ottevaere

This paper is the first part in a series of three where the authors show how photonics based food sensors can contribute to the quality control and safety of solid and liquid food products. In this first part, we describe the theoretical aspects of the various physical phenomena that can occur during food screening together with their related measurement setups. In addition, this document contains information regarding data processing and the concerned sensing platforms.

Introduction

Food quality and food safety are gaining more and more importance in recent decades. In particular, application domains have expanded, such as the identification of foreign bodies in solid food streams, the quality of screening of vegetables and fruits, the recognition of food products inducing a health risk and the monitoring of the quality and authentication of liquids. Solid food sensing methods are often insufficient in the sense that they are error sensitive and time consuming, caused by the manual or chemical, sample based screening of the products. For most liquids a decent monitoring method is missing. In view of this, the authors of this paper started exploring the potential use of photonics where the main objective consisted of answering the question of whether food screening methods could be photonics based. This series of articles provides an overview of our research of the past eighteen years.

Theoretical Aspects

The optical measures applied to decide upon food quality, identity, and safety are linked to the different physical processes that ensue when a light wave hits a biological substance. Fig. 1 gives a schematic view of the different types of interaction of an incident electromagnetic wave with the inside and on the surface of the sample. The interactions cause: selective absorption; molecular vibrations; elastic scattering leading to bulk scattering; refraction; specular reflection; diffuse surface reflection; and fluorescence. Both one-photon induced fluorescence (OPIF) and two-photon induced fluorescence (TPIF) can occur.

Selective Absorption

Selective absorption occurs when the energy of the incident light waves corresponds to one of the excitation states of the biological substance. The electrons are brought to a higher energy level. In a time scale of approximately 10^{-12} s, this energy is lost via thermal emission by collisions. Pigment molecules of vegetables and fruits show resonances in the visible part of the electromagnetic spectrum (380 to 780 nm) due to their conjugated structure that consists of long chains with alternating single and double chemical bonds. The energy needed to bring the mobile, delocalized pi-electrons into an excited state corresponds to the energies of visible photons. The more conjugated double bonds in a system, the longer the wavelength of the absorbed light.

Based on their structure, formula pigments are typically classified into three main groups: phenol derivatives, carotenoids, and chlorophylls and are further classified in a number of subgroups [1]. Table 1 gives an overview of the most common pigments with their corresponding absorption bands and appearance in vegetables and fruits. The displayed table assembles the outcome of a literature survey supplemented with our own experimental verifications. Based upon information in food tables [2], we determined which pigments are present in a specific food product. Next, we performed a literature survey with the aim to obtain knowledge on the most distinct absorption bands for the mentioned pigments. The outcome was a list with absorption bands for each pigment. Although, for most of the pigments, these were the bands observed for *artificially generated* samples where, for example, the pure pigment was dissolved in a medium. In addition, one food product contains multiple pigments with sometimes overlapping bands. Therefore, we experimentally verified the appearance of these bands in real food products where it consisted in measuring the absorption spectrum and determining the absorption bands of the calculated second derivative spectrum (see Data Processing).

Through the years, different *test equipment* setups were applied to measure the absorbance spectra of solid and liquid products following new developments in spectroscopic

1094-6969/16/$25.00©2016IEEE

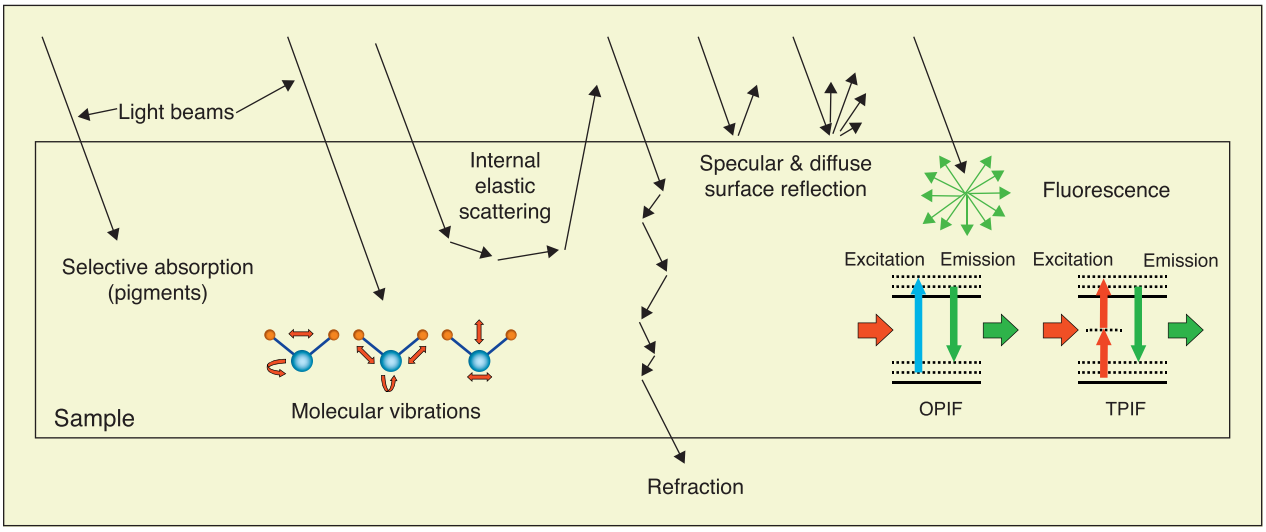

Fig. 1. After interaction of a light beam with a biological sample, different phenomena take place. The most significant are selective absorption, molecular vibrations, internal elastic scattering, refraction, specular and diffuse reflection at the surface, and fluorescence.

equipment and accessories. The absorbance spectra are calculated from the recorded reflection spectra by applying Lambert–Beer's law.

All systems for measuring the absorbance of solid products have two main parts in common: the spectral broadband light source at the illumination side and an optical spectrum analyzer at the receiving side. Both devices are fiberized. In most cases, we use a combined deuterium-halogen source that emits between 250 to 2000 nm (LS500-100-Instrument Systems). The additional lens positioned at the end of the output fiber bundle collimates the light to a beam diameter close to 5 mm. The use of this source is preferred because of its high output stability; variations in the emitted spectral emittance are below 2% after a warming up time of 30 min. If a detector array spectrum analyzer is used to record the spectrum, a less stable (but much cheaper) spectral broadband light source can be applied. In those cases, the source spectrum must be captured prior to each sample measurement.

Depending on the light source, we used two types of optical spectrum analyzers: a high-end apparatus (Spectro 320–Instrument Systems) characterized by a high spectral resolution (picometer range) and lower resolution portable devices (AvaSpec 3648-Avantes) with an optical resolution of 1.4 nm. The measurement procedure of the high-end apparatus corresponds to an automatic scanning of the spectrum, resulting in measurement times between 1 to 15 min. Portable spectrometers, on the other hand, measure the spectrum in real-time with measurement times of a few seconds. The signal is diffracted into the separate wavelength components and focused on a silicon detector array inside the apparatus. For the high-end device, the light is diffracted towards a single detector at a fixed position. Since the instrument employs a photomultiplier tube for the UV-VIS region (and an InGaAs detector for the NIR region), the scanning-based apparatus is more sensitive compared to the portable device.

In addition to the differences in measuring devices, dissimilarities in measurement geometry also exist. Vegetables and fruits are optical non-homogeneous materials in which the coloring pigments are randomly embedded in the dielectric material. These types of materials fulfill the so-called *dichromatic reflection model of Shafer* [11] that independent from the illumination and detection arm, the light reflected from a non-homogeneous dielectric object is the sum of two values which correspond to the interface and the body reflection. Since the index of refraction of the surface material is constant in the visible part of the spectrum, the specular reflected light has the same color as the source. However, the body reflection, which is the light scattered from the product after penetration inside the product, will be strongly colored. As such it is important to isolate the body reflection from the surface reflection.

In the setup shown in Fig. 2a, both the illumination and detector arm are mounted such that the incident and the detection angle can be adapted. Typically we consider an illumination angle of -45° and a detection angle of 0°. In this configuration, an additional lens system is mounted between the illumination fiber and the product for focusing the incident light. The receiving fiber bundle which guides the light to the spectrum analyzer has an acceptance angle ϕ of 36.9°. To minimize variations in sample position, the samples are placed on a plate with a hole and illuminated from the bottom side. By rotating the plate, multiple samples can be measured successively.

An alternative setup is shown in Fig. 2b where the illumination and detection light are guided through a so-called reflection probe (FCR-7xx200-2 - Avantes). Six illumination fibers are used for sending light from the spectral broadband light source to the sample so that reflection can be measured with the help of a seventh fiber present in the center of the reflection probe tip. A spectrometer is coupled to this central fiber. We position the probe 45° perpendicular to the sample surface to avoid measurement of specular reflected components.

In some exceptional cases, we make use of the setup shown in Fig. 2c where we position the solid sample at the entrance

Table 1 – Classification of some vegetables, fruits, and seafood by pigment types, absorption region, color, and peak absorption

Main class	Phenol derivatives				Carotenoids									Chlorophylls	
Sub-class	Flavonoids		Betalaines		Carotenes			Xanthophylls						Chlorophylls	
Pigment name	Anthocyanin	Anthoxanthin	Betacyan	Betaxanthine	α-carotene	β-carotene	Lycopene	Astacene	Astaxanthine	Cryptoxanthine	Canthaxanthin	Luteine	Zeaxanthine	Chlorophyll a	Chlorophyll b
Color	purple	orange-yellow	violet	yellow	orange	orange	red	red	orange-red	orange-yellow	orange-yellow	orange-yellow	yellow	green	green
Peak absorption (nm)	500-545		480	536	463	426, 448, 456, 474, 485	444, 473, 502	473	468	453	467-470	445	454	430, 662	453, 642
Reference	[3]	[4]	[5]	[6]		[7]	[8]	[9]						[10]	
Pigment types in some vegetables, fruits, and seafood															
Apricots					x	x	x						x		
Bell pepper							x							x	x
Berlotti beans					x	x						x		x	x
Blackberries	x														
Broccoli					x	x						x		x	x
Brussels sprouts					x	x						x		x	x
Carrots					x	x						x			
Cauliflower		x												x	x
Celery														x	x
Cranberries	x														
French beans					x	x						x		x	x
Garden beans					x	x						x		x	x
Leeks														x	x
Lettuce					x	x						x	x	x	x
Maize													x		
Mushrooms		x													
Mussels											x				
Onions		x													
Olives														x	x
Oranges						x				x		x	x		
Peas					x	x						x		x	x
Potatoes		x			x	x						x			
Prunes					x	x				x		x	x	x	x
Raisins														x	x
Red currants	x														
Shrimp								x	x		x			x	x
Spinach					x	x								x	x
Strawberries	x													x	x
Tomatoes						x	x								
White cabbage					x	x							x		

port of a reflectance integrating sphere (AvaSphere-30-REFL-Avantes) and connect the two ports to the source and the optical spectrum analyzer. This allows the calculation of absolute absorbance values since all of the reflected light is captured. However, the large number of side wall reflections strongly diminishes the intensity of the detector signal. All reflectance spectra were measured against a 99.9% spectralon diffuse reference standard (SRS-99–Labsphere).

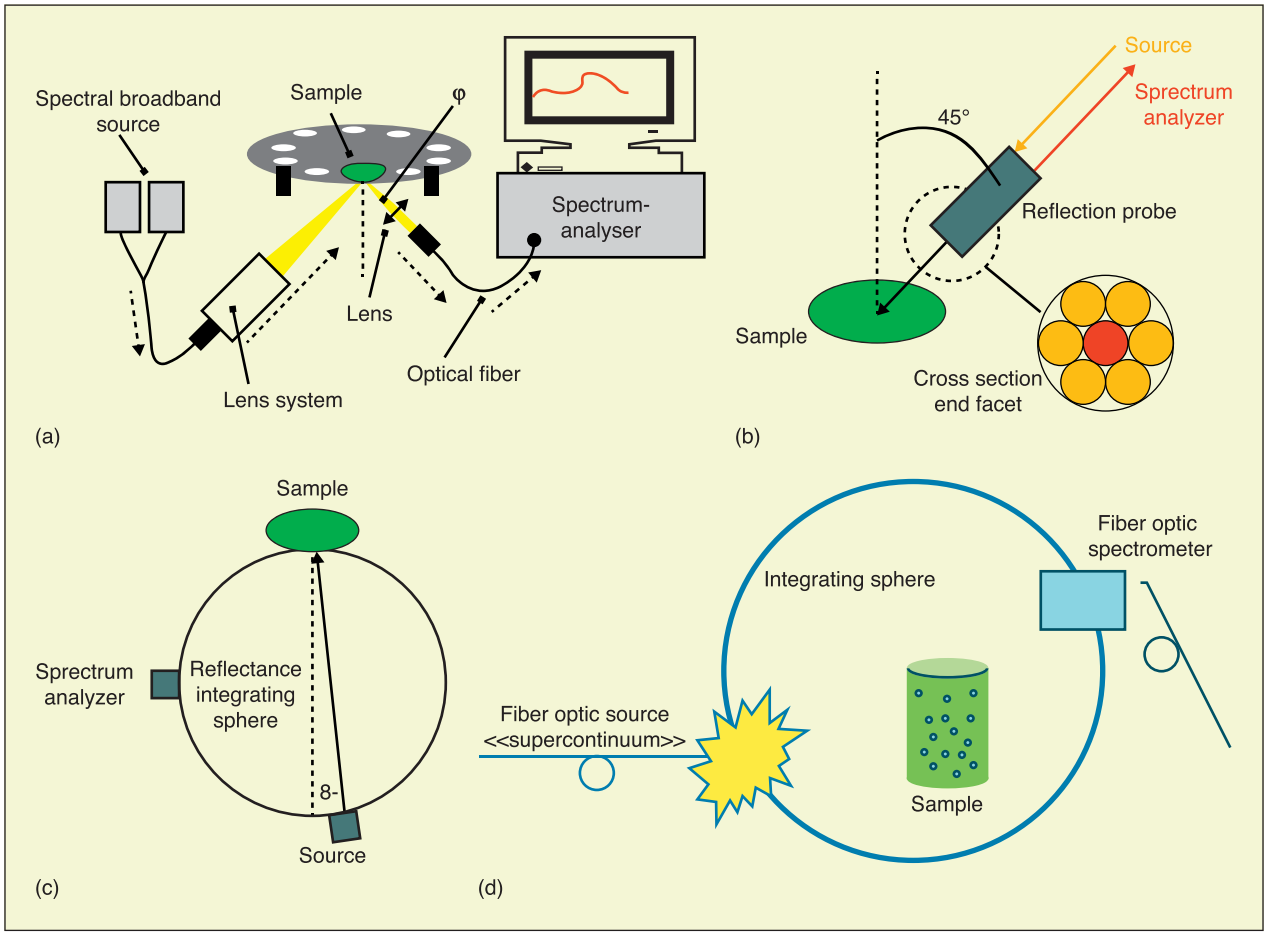

Fig. 2. Absorption spectroscopy setups: (a) on solids by means of a customized laboratory setup; (b) by using commercially available components including a reflection probe; (c) by a reflectance integrating sphere, which allows the measurement of absolute absorbance values; and (d) diffuse-light absorption spectroscopy by means of optical fiber technology [11].

When carrying out *absorption spectroscopy in liquids*, the measurements are often influenced by dispersed scattering particles that cause turbidity. Scattering dependence is the main drawback of absorption spectroscopy, especially when particles settle down or change their position in time. For this reason, liquids must be filtered prior to measurements with a consequent loss of time and increased cost. *Diffuse light absorption spectroscopy* can overcome this scattering dependence problem [12]. This spectroscopic technique makes use of an integrating sphere which contains the sample under test. The source and the detector are butt-coupled to the sphere. Almost all of the light impinging on the sphere surface is diffusely reflected, and the detector can be placed anywhere in the sphere to gather the average flux [13]. By inserting an absorbing medium in the cavity, a reduction of the radiance in the sphere occurs. The reduction is related only to the absorption of the sample and to its volume, and is independent of scattering, which does not change the average radiance in the cavity.

Efficient diffuse light measurements need bright sources. A conventional deuterium/halogen lamp is enough, provided that it is butt-coupled to the integrating sphere. However, when optical fibers are needed for a better geometrical versatility of the measuring system, conventional lamps provide poor and insufficient light intensity. To overcome insufficient lighting, we used a compact, high brightness supercontinuum fiber optic source, the revolutionary advent of which has recently changed the perspectives of optical spectroscopy [14], [15]. The Fianium-SC400 fiber optic supercontinuum source was used for illumination; it emits 4 W throughout the entire 415 to 1800 nm spectral range. The Instrument Systems Spectro 320 fiber optic spectrometer was used as the detector and scanned the wide 400 to 1700 nm spectral range with a resolution of 1.37 nm. The Labsphere LMS100 cavity was used as a diffusing sphere, the ports of which were equipped by means of fiber optic connectors for coupling to both the source and the detector. Fig. 2d shows a schematic of the setup for diffuse light absorption spectroscopy by means of optical fiber technology.

Molecular Vibrations

If the photon energy of the incident light is insufficient to excite the electrons to a higher energy level, molecular vibrations can occur. The near-infrared spectrum (750 to 2500 nm) represents a complex spectrum of combination and harmonic tones caused by the multitude of existing eigenmodes. Vibration modes are categorized either as bending or stretching modes. Most of the vibrational bands appearing in the near-infrared

Table 2 – All basic building blocks of food products have multiple distinct absorption bands in the near infrared part of the electromagnetic spectrum

Cellulose (nm)	Oil (nm)	Proteins (nm)	Starch (nm)	Sugar (nm)	Water (nm)
978	1161	909	918	978	958
1363	1212	1018	979	1380	1409
1460	1387	1143	1700	1437	1460
		1187			
		1485			
		1690			

region originate from stretch movements of a limited number of functional groups: C-H, O-H, N-H, C=O, C-O-H and H-O-H, which correspond to the basic building blocks of the food products: water, oil, starch, cellulose, proteins and sugar. Table 2 displays the spectral positions of the most distinct absorption bands for the feed components in the near-infrared region (800 to 1700 nm).

Only the strongest bands appearing in the range 800 to 1700 nm are displayed. Vibration spectra are measured with a setup equal to the one applied to measure absorption spectra.

Internal Elastic Scattering

When the incident light wave is neither selectively absorbed nor absorbed via molecular vibrations, internal elastic scattering occurs leading only to a change in light direction. The light will appear as scattered light at the surface of incidence or as transmitted light (refraction).

To study the internal scatter patterns of solid food products, we have so far applied three different configurations. The first setup permits the measurement of the cosine corrected Bidirectional Scatter Distribution Function (ccBSDF) commonly applied whenever both surface and bulk scattering is present [16]. The ccBSDF is calculated via the following formula:

$$\mathrm{BSDF} = \frac{P_S}{P_i\ \Omega \cos \Theta_S} \tag{1}$$

with P_i equal to the incident power, Ps the scattered power under an angle θ_s and Ω the detector's solid angle. The sample under test is positioned at the intersection point of the illumination and detection arm. Both arms can be rotated around this point such that the scattered light intensity can be measured for different illumination and scatter angles to determine the ccBSDF values. This setup induces a high degree of flexibility. The design of the rotation table allocates a rotation resolution of 0.5°. Moreover, this setup allows the implementation of different types of light sources (lasers or a supercontinuum source for example the 4W SC400-Fianium) and detectors (standard silicon optical power meters or optical spectrum analyzers). Disadvantages include the time-consuming measurements.

To have a quick but less quantitative access to scatter profiles, we built a second setup. This configuration images the scattering onto a camera. Again, any type of light source can be put into operation. Two previous setups measured the scattered light coming from the intersection point between the illumination and detection arm. In some cases, it is desired to also capture the light from the surrounding area inside the product. For the third setup, the illumination arm is rotatable with the position of the sample as the rotation center. The detection arm is mounted on a translation stage driven by a motion controller to scan the scattered light along the object's surface (850G linear actuator and ESP300 motion controller-Newport). The device is characterized by a movement accuracy of 1 µm. Light sources and detection devices are equal to those of the first described setup. Additional optics must be applied to enlarge or focus the beams. Targeted illumination spots are typically smaller than 2 mm. The surface area from which scattered light is captured is close to 3 mm^2.

Refraction

To measure the intensity and scatter profiles of refracted light beams, we typically use two different setups, which each use a laser source to ensure that the transmitted light exceeds the detection limits of the detector. To determine the transmittance, both the incident (P_{in}) and the transmitted (P_{out}) light must be measured. This is accomplished by using a beam splitter and two optical power meters. The transmitted light is collected by a lens. To measure the transmitted scatter profile we image the transmitted beam onto a CCD camera (SP620-Ophir Spiricon). At the illumination side, we apply a Keplerian beam expander to tune the transmitted beam diameter to the dimensions of the active area of the detector. In addition, we add a pinhole at the focus of the first lens to spatially filter the laser beam.

Specular and Diffuse Surface Reflection

Yet another phenomenon is surface reflection. In the case of *specular reflection*, the reflected light is concentrated in a small cone of light; diffuse reflection on the other hand reflects the light towards a broader range of angles. Analysis of the polarization state of the light reflected from a sample under test illuminated with a polarized light beam allows the separation of both contributions. The pattern that appears depends on the surface roughness. For small variations ($\sigma < \gamma$) the occurring one-fold reflection defines the surface as being optically flat. In this situation the polarization state of the incident light is nearly maintained. Multiple reflections take place for an increased number of surface fluctuations ($\sigma > \gamma$). In this circumstance the (linear) polarization state of the incident light changes to an elliptic polarization state. The degree of

depolarization increases with the number of reflections. A final (diffuse) surface reflection phenomenon is Rayleigh and/or Mie scattering from surface particles.

In summary, four different phenomena contribute to the observed scatter pattern: specular reflection at the optical flat parts of the surface, diffuse reflection (surface scattering) from rough surface parts, Rayleigh and Mie scattering from surface particles and scattering inside the product described earlier. From these four phenomena only the specular reflection and Rayleigh and Mie scattering will polarize or maintain the incoming polarization state. Studies have demonstrated that the appearances of both events are product dependent. All types of stalks and stems show a high degree of specular reflection. Several food products including apples, cabbages, and raisins are characterized by a thin powder film at their surface [17] that induces Rayleigh and Mie scattering.

Surface Light Reflection

To study the polarization properties of the light reflected at a sample's surface, a linearly polarized laser beam illuminates the sample. The polarization direction is perpendicular to the incident plane (s-polarization). The light reflected around the specular direction is focused onto the measuring head of a commercial polarization analyzer (RPA2000–Instrument Systems). The dimensions of the setup prompt an acceptance angle smaller than 5°. The rotating analyzer measures the optical power for different angular positions. From these measures, several parameters are calculated. All of the parameters are related to the polarization state of the measured light beam (including the Stokes parameters, the elliptical polarization, and the degree of linear polarization).

Fluorescence

In fluorescence, light is absorbed and reemitted (at a time scale of several nanoseconds to microseconds) at wavelengths dissimilar from the excitation wavelength. The energy of the excitatory photon(s) must be sufficiently high to bridge the energy gap between the ground state and the state from which the fluorescence light is emitted. Excitation can be induced via the absorption of one photon or via the simultaneous absorption of two photons, referred to as one-photon induced fluorescence (OPIF) and two-photon induced fluorescence (TPIF), respectively. In the latter case, the electron reaches the high-energy state via an intermediate virtual state. Since emission arises in both cases from the same excited state, the fluorescence spectra are alike. OPIF measurements typically apply an excitation wavelength from the ultraviolet or visible part of the electromagnetic spectrum, while for TPIF measurements the excitation wavelength is shifted towards the near-infrared region. The non-linear character of the two-photon absorption process gives rise to fluorescence intensities, which are several orders of magnitude weaker (~ factor 100) compared to the OPIF outcome.

When fluorescing substances are present in food products, they are classified into two groups: substances with a natural occurrence or contaminations. The first group includes the green pigment chlorophyll, the amino acid tryptophan, and the protein riboflavin. An important group of contaminants is the mycotoxins, which are toxic compounds that grow on specific fungi under a diverse range of environments. Between 300 and 400 different mycotoxins are known today. Only three of them show fluorescence: aflatoxins, ochratoxin A and citrinin [18]. Fig. 3 compares the fluorescence spectra of chlorophyll, tryptophan [19], riboflavin and aflatoxin. The spectral overlap between the natural fluorescing substances tryptophan and riboflavin and the contamination aflatoxin is clearly visible.

Through the years different available laser systems have been used to excite fluorescence. These include an argon laser system (Spectra Physics), a mode-locked Ti-sapphire laser system (Tsunami- Spectra Physics) combined with a flexible harmonic generator (GWU-FGH-Spectra Physics), HeNe lasers and semiconductor lasers (InGaN, InGaAlP). For TPIF an additional lens is mounted between the laser and the sample under test to increase the power density to the required level to provoke TPIF. The sample is excited from the bottom side and is positioned onto a motion controlled translation stage allowing the scanning of the sample. The emitted fluorescence light is collected by a lens which couples the light into an optical fiber connected to the optical spectrum analyzer. Two types of spectrum analyzers available in our labs can be used: the scanning-based spectrum analyzer earlier described (Spectro 320–Instrument systems) and a portable, detector array based analyzer (AvaSpec2084–Avantes). The latter is able to measure real-time fluorescence spectra between 300 to 1100 nm with an optical resolution of 8 nm. However, the much slower scanning-based device contains an adjustable slit wheel and a more sensitive detector (PMT) in the visible part of the spectrum.

Data Processing

Absorbance Calculation and Second Derivative Spectra

The linear relation between the absorbance A and the concentration of the absorbing component c is given by Lambert-Beer's law [20]:

$$A = \log_{10}\left(\frac{1}{R}\right) = abc \tag{2}$$

where a is a proportional constant and b is the thickness of the measured sample. For solid food products this law is not valid since light scattering alters the optical path length. Therefore, a more realistic version of the Lambert-Beer law is:

$$A = A_0 + abc \tag{3}$$

in which A_0 is a value representing the background scattering. Elimination of A_0 is accomplished by calculating the second derivative spectrum. A second advantage of working with derivative spectra is the enhanced visibility of overlapping absorption bands. The second derivative spectrum contains a local minimum for every peak that appears in the original spectrum, although each derivation increases the signal-to-noise ratio.

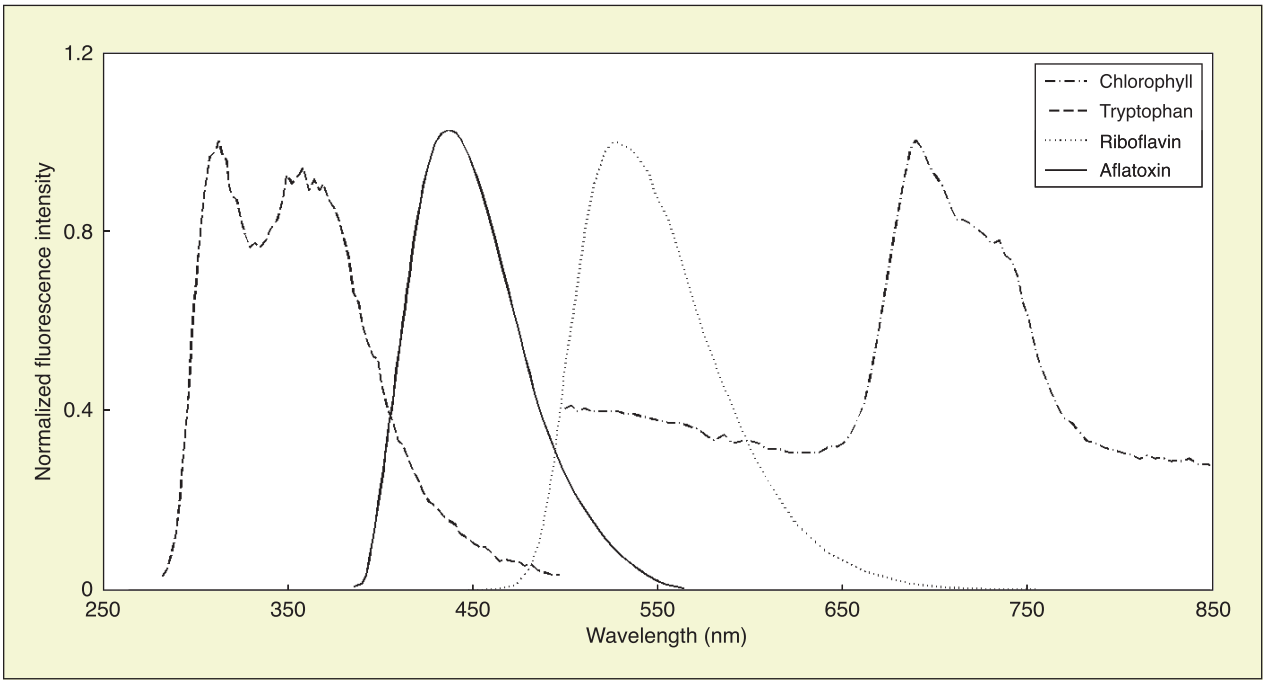

Fig. 3. Food products fluorescence in the region 250-850 nm. The spectral overlap between the natural fluorescing substances tryptophan and riboflavin and the contamination aflatoxin is clearly visible.

Color Calculation

The color of an object can be calculated and visualized in different color systems. We use the CIE1931 color system which represents all visible colors by two chromatic values x and y. A representation in the xy-plane results in the typical horseshoe-shaped CIE chromaticity diagram [21]. Starting from the reflectance spectrum $R(\lambda)$ we use the color matching functions $\overline{x}$, $\overline{y}$, and $\overline{z}$ to calculate an object's color under a certain light source. For this we multiply the reflectance spectrum $R(\lambda)$ with the emission spectrum of the source $S(\lambda)$ and multiply the resulting spectrum separately with each of the three color matching functions. Integration of the three spectra (between 380 to 780 nm) leads to three values X, Y, and Z. After normalization, the color is represented in the 2-D xy-plane.

Class Difference

The quantitative value we will use to describe the performance of a certain optical measure f is the class difference D. This value is a measure of the difference between the average values μ of two product classes i and j, taking into account the standard deviation σ and the amount of measured samples N. The class difference is calculated by applying following formulas:

$$D_{fij} = \frac{\left|\mu_{fi} - \mu_{fj}\right|}{\sqrt{\sigma_{fi}^2 + \sigma_{fj}^2}} \quad for\, N > 30 \tag{4}$$

$$D_{fij} = \frac{\left|\mu_{fi} - \mu_{fj}\right|}{\sqrt{\frac{\sigma_{fi}^2}{N_1} + \frac{\sigma_{fj}^2}{N_2}}} \quad for\, N < 30 \tag{5}$$

Sensing Platforms

The optical measures that are the outcome of the spectroscopic research are implemented in a practical detection platform.

For the solid products, we implement a commercial commonly applied scanning-based monitoring system, which is able to screen each individual artefact (Fig. 4). While the samples are travelling over a conveyor belt at a speed of several tons/hour, the products are optically screened. A few milliseconds after an unwanted product is detected, it is hit by timed, high-speed air guns and removed. Only the good product continues in the production line. The basic building blocks of the optical scanning platform are the laser source and a polygon mirror responsible for the scanning. The small illumination spots attributed to the use of a laser source allow the detection of small defects with dimensions as small as 1.5 mm.

For each application, we build a *static* proof-of-concept demonstrator, which is representative of a commercial optical platform in terms of the distance of the illumination and detection unit to the product under test. In this setup, test measurements can only be performed for one scanning line.

For liquid samples, we employ an on-line monitoring system consisting of a fluidic channel through which the liquid under test can flow during optical detection with commercial measurement equipment. If we want to remove the bulky and free-space optical hardware that is currently used in conventional bench-top measurement systems and also enhance the sensitivity and stability of the measurements to realize a significant size reduction, a first step towards portable detection instruments can be made. By combining the fluidic and optical functionalities onto one chip, we achieve a so-called optofluidic chip [22].

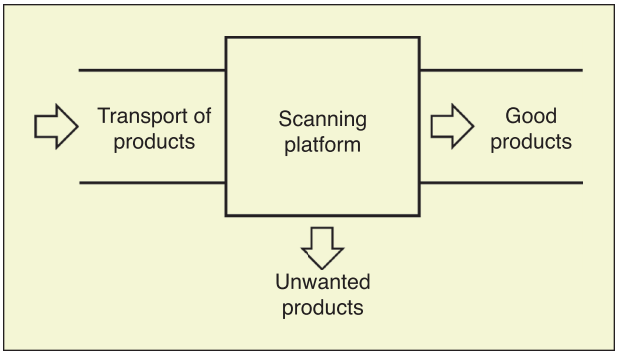

Fig. 4. The optical measures defined for the solid samples are implemented in a scanning-based in-line monitoring system.

Typically nanoliter sample volumes are processed and manipulated using microfluidic channels that range in size from tens to hundreds of micrometers. This downscaling offers the potential of a fast response time, low sample and reagent consumption, enhanced reliability and sensitivity through process automation, parallelism on a single substrate, portability, disposability and opportunities for low-cost mass production. Portability allows analyses to be done outside the laboratory, minimizing the risk of sample contamination and degradation, offering faster response on the spot and at a lower cost. Such optofluidic devices are suited for applications where real-time and on-site or in-line testing is beneficial, as in: food quality control and industrial analysis, biochemical analysis in point-of-care testing, and environmental monitoring of e.g., wastewater, biodefense and forensics.

Therefore, it is important to make versatile optofluidic chips, which can easily be reconfigured for sensing a large variety of molecules at different wavelengths. At the same time, we want to focus on the use of plastic micro-optical components because they hold the promise of mass manufacturing using replication techniques at low cost. We will also try to develop micro-optical detection systems with a high sensitivity that feature at the same time a relatively simple layout to ensure manufacturability and robustness. Last but not least, we want to ensure that these systems can be used outside the laboratory environment, for e.g., food quality monitoring, and that they can be manufactured using standard fabrication techniques. Therefore, we have designed the systems so they are insensitive to reasonable fabrication and misalignment errors [22].

In this article, we show a multi-measurement system that incorporates a robust and optofluidic chip that is compatible with low-cost replication. This system is capable of simultaneous absorbance (ABS) and laser-induced fluorescence (LIF) analysis. In addition, a simultaneous scattering measurement is performed so that information about a sample's turbidity can be acquired.

Spectral data obtained through optical spectroscopy often contains a lot of redundant data. Through multivariate data analysis, it is possible to summarize extensive spectral data in a small number of latent variables. Furthermore, it is also possible to use multivariate data analysis to set up predictive models for relevant quality parameters of the sample under test. From the composition of these latent variables, it is possible to derive excitation wavelengths at which the most significant variations (in general, or with respect to a specific quality parameter) are observed. For the various food samples such as vinegars and oils, we found that an optical measurement at both 405 nm and 450 nm was most suited [23].

Our proof-of-concept demonstrator consists out of an optofluidic chip. The output of the 405 nm and 450 nm laser diodes is conditioned to achieve two collimated excitation beams. These collimated beams are then combined to a dual wavelength excitation beam using a right angle mirror and a dichroic mirror. This beam is then sent into an optical detection assembly that holds the optofluidic chip shown in Fig. 5a. The excitation light will interact with the sample that is contained inside the chip's fluidic channel. The excitation light that is not absorbed leaves the chip through its output facet. The non-absorbed light then travels through a 50:50 beam splitter towards the absorption photodetectors, each equipped with a 405 and 450 nm bandpass filter (Thorlabs FB405-10 and FB450-10). The photomultiplier tubes (PMT) are placed on the top and bottom sides of the chip to capture scattered light or fluorescence, respectively. The top PMT that is used for measuring fluorescence is preceded by a 500 nm long pass filter (Thorlabs FEL500). The bottom PMT that detects scattered light is fitted with a 405 nm bandpass filter. The optofluidic chip is clamped in place by the optical detection assembly and simultaneously provides a leakage free interface between the on chip fluidics and the external fluidic system.

The proof-of-concept demonstrator setup is fully controlled by a PC running NI LabVIEW. This way, the experiments and the external fluidics (pumps and injection valve) are fully automated. In conjunction with a NI CompactDAQ analog-digital interface, the aforementioned program generates the modulation waveforms for both excitation lasers and simultaneously samples the signal of the detectors. The lasers are time-multiplexed and modulated by a sine wave at 1 kHz. By means of fast Fourier transform (FFT), the signal component at 1 kHz is recovered for each photodetector. This way, noise reduction is achieved, boosting the sensitivity of our multi-measurement system and offering a low-cost alternative to making use of a lock-in amplifier [23].

As shown in Fig. 5a, the optofluidic chip has a W-shaped channel. For this geometry the excitation beam propagates perpendicularly through the channels. This way, air bubbles will only cross the excitation beam shortly while propagating through the channel. Thus, their influence on the signal response is shortened in time. Because of this, the envelope of the signal response will exhibit short spikes rather than the complete destruction of the envelope. Such spikes can be removed by post processing the signal responses, reducing the influence of air bubbles even more. The channels have a depth of 900 μm and a width of 1-mm with 1-mm of separation between neighboring channels. The channel height also guarantees that the complete beam waist of the excitation beam can be coupled in. The entry and exit facets are given the same height for the same purpose. The polymer chip is mass manufacturable through a master

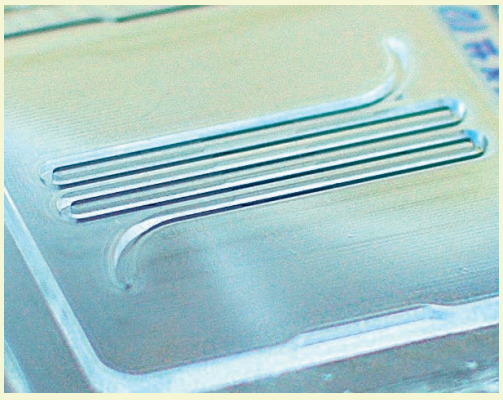

(a)

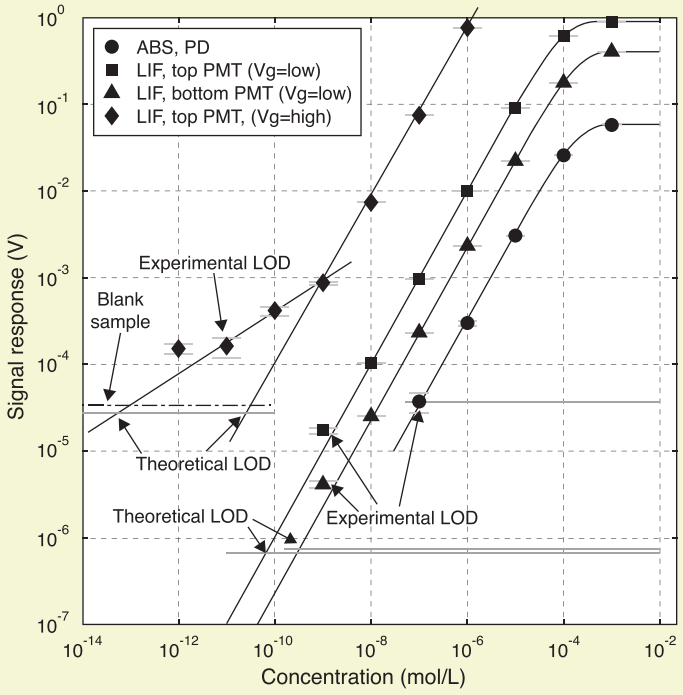

(b)

Fig. 5. (a) W-shaped channel on an optofluidic chip in PMMA. (b) Coumarin 480 Calibration curve. Each curve is accompanied by a flat line that represents 3.3 times the noise level of that detection channel. At the intersection of this level and the fitted curve the theoretical LOD is found [23].

mold that is machined in brass by milling and ultra-precision diamond tooling and replicated by hot embossing. By ensuring that the chip can be replicated by means of hot embossing, we ensure that in a later stage low-cost mass manufacturability is guaranteed, and that the chip can be fabricated in a wide variety of thermoplastic polymers such as cyclic olefin (co)polymers.

Given that the on-chip fluidic channel is 1-mm wide, every extra fold increases the chip's sensitivity as the interaction length is increased by 1-mm. We have decided to fabricate a chip with an interaction length of 5 millimeters, i.e., this chip will have a W-shape channel that contains 5 folds or plies. This choice offers a good compromise between sensitivity, internal volume, and rinsing time.

To determine how well our optofluidic system works, we perform two calibration experiments prior to its use for food analysis. The first experiment involves setting up a calibration curve for the detection of Coumarin 480 dissolved in ethanol. Coumarin 480 is often used as a benchmark sample for microfluidic systems [23]. The second experiment investigates the system's sensitivity to turbidity. A calibration curve for turbidity standards is setup, and the correct operation of the scattering measurement is verified.

We measure the response of a series of samples of Coumarin 480 (Exciton) dissolved in ethanol (Technisolv 99%). We start by making 50 ml of stock solution with a concentration of 10^{-3} mol/L. From this stock solution, we subsequently mix every subsequent sample diluting by a factor of ten. As such, we obtain 10 solutions ranging from 10^{-3} mol/L down to 10^{-12} mol/L. For this series of samples, we will setup a calibration curve for ABS and LIF detection using 405 nm excitation. The susceptibility of Coumarin 480 to 450 nm excitation is very limited, and so we will only be using the 405 nm excitation laser for this experiment. For this purpose, the top PMT and bottom PMT are both fitted with a 500 nm longpass filter, and the photodetector for the absorbance analysis is fitted with a 405 nm bandpass filter. For these experiments, the sample volume of 158 ml is injected at a flow speed of 9 ml/s.

In the first experiment, we configure the gain voltages of the PMTs such that the system can observe the signal response without overdriving their respective programmable gain amplifier (PGA) set to unity. The goal of this first experiment is to see how well the system can measure small concentrations while still being able to measure large concentrations (1-mM) as well. In a second experiment, the gain voltage of the top PMT is increased to improve the performance of the detection of small concentrations. The goal of this second experiment is to determine the empirical limit of detection.

Fig. 5b shows the plotted results of the low and high gain experiments. Every calibration curve also shows the signal level equal to 3.3 times the background noise as a horizontal line in the plot. When applying a fit to the calibration curves, it is the intersection with the aforementioned detection level that determines at which sample concentration lies the theoretical limit of detection. The background noise has a different value for each respective measurement channel.

The results of the first experiment are shown with the three rightmost curves and their respective fitted functions. The

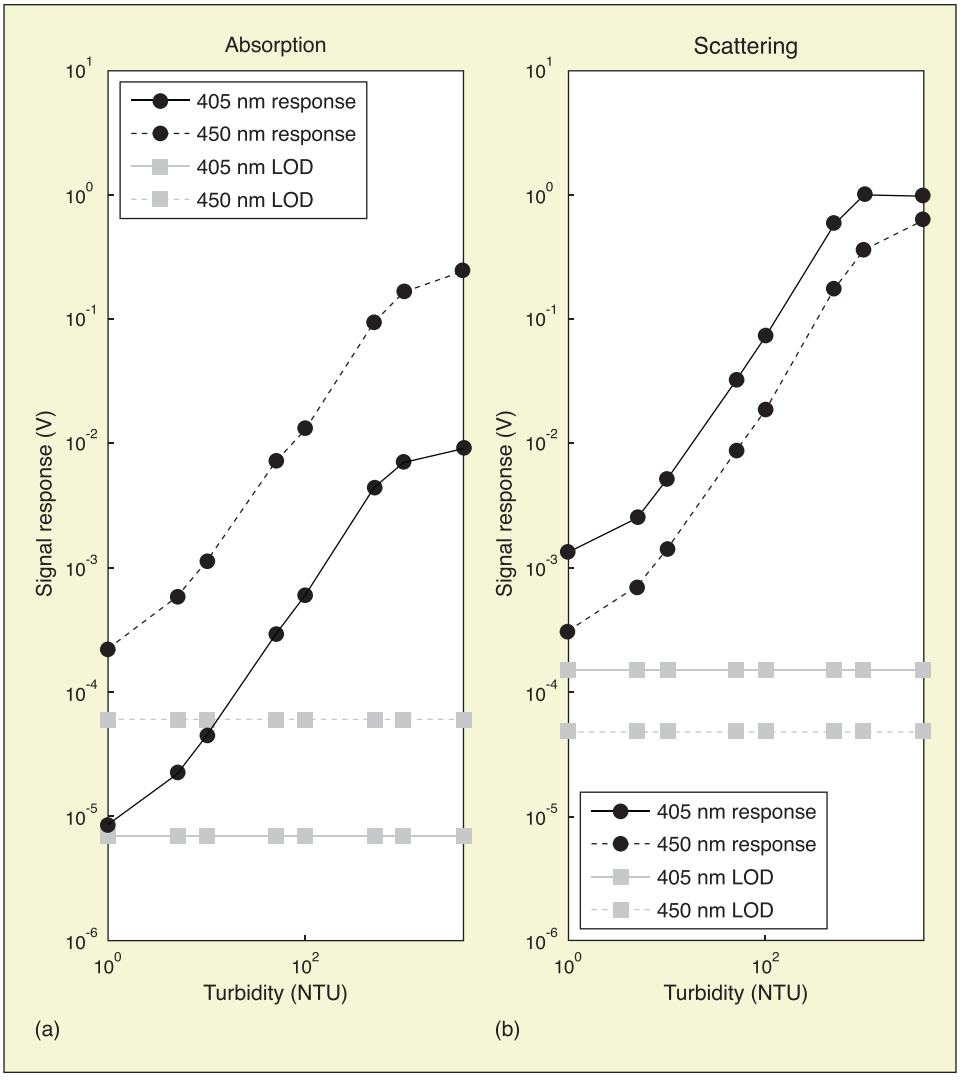

Fig. 6. Turbidity calibration curve for both 405 nm and 450 nm [23].

top and bottom PMT theoretical limits of detection of 3.26×10^{-11} mol/L and 6.34×10^{-11} mol/L, respectively, are found. For the second experiment, with the top PMT having an increased gain voltage, we yield a theoretical LOD of 3×10^{13} mol/L. At low concentrations (below 10^{-11} mol/L), we observe that the system is suffering from electronic noise.

Next, we calibrate our system's response to several Fluka Polymer Bead Turbidity Calibration Standards with a known turbidity value. The studied sample range consists of 1, 5, 10, 50, 100, 500, 1000, and 4000 NTU calibration standards. For this experiment, we use both the 405 nm and 450 nm laser diodes as excitation sources. Fig. 6 shows the results of this calibration experiment.

The Fig. 6a graph shows the calibration curves for the absorption measurement, and Fig. 6b does the same for the scattering measurement. For all curves we observe, there is a clear correlation between the observed signal level and the sample turbidity. Furthermore, this relation has a clear inverse function, with the exception of the 4000 NTU scattering data point for 405 nm excitation. The latter is due to saturation of the PMT and can be avoided by lowering the PMT's gain voltage. Both the absorption and scattering graphs also show the LOD level for each detector equal to 3.3 times the background noise σ_B.

General Conclusion

This paper shows that photonics based food sensors can definitely contribute to the enhancement and safety of both solid and liquid food products, especially for the identification of foreign bodies in food streams, the quality screening of solid food products, the identification of food products inducing a health risk, and the quality monitoring and authentication of liquids. With the help of ten concrete case-studies covering these four application domains, we will demonstrate in parts 2 and 3 the usefulness of optical screening methods in general and define for each application in particular the corresponding optical measures.

Acknowledgment

For help with the calibration of the optofluidic chips, the authors would like to thank Tom Verschooten (VUB TONA).

References

[1] I. S. University, "Course Notes Food Science and Human Nutrition - FS HN 311: Food Chemistry." 2016. [Online]. Available: http://catalog.iastate.edu/azcourses/fs_hn/.

[2] World Food Programme, "Food Composition Table." [Online]. Available: http://www.wfp.org/fais/nutritional-reporting/food-composition-table.

[3] M. N. Merzlyak and O. B. Chivkunova, "Light-stress-induced pigment changes and evidence for anthocyanin photoprotection in apples," *J. Photochem. Photobiol. B Biol.*, vol. 55, no. 2–3, pp. 155–163, May 2000.

[4] M. Megala and B. J. M. Rajkumar, "Theoretical study of anthoxanthin dyes for dye sensitized solar cells (DSSCs)," *J. Comput. Electron.*, vol. 15, no. 2, pp. 557–568, Jun. 2016.

[5] J. Soriano-Santos, M. Franco-Zavaleta, C. Pelayo-Zaldivar, M. Armella-Villalpando, M. Yanez-Lopez, and I. Guerrero-Legarreta, "A partial characterization of the red pigment from the Mexican fruit cactus 'jiotilla,'" *Rev. Mex. Ing. Quim.*, vol. 6, no. 1, pp. 19–25, 2007.

[6] M. Wendel, D. Szot, K. Starzak, D. Tuwalska, J. Gapinski, R. Naskrecki, D. Prukala, M. Sikorski, S. Wybraniec, and G. Burdzinski, "Photophysical properties of betaxanthins: Vulgaxanthin I in aqueous and alcoholic solutions," *J. Lumin.*, vol. 167, pp. 289–295, Nov. 2015.

[7] T. Polivka, C. A. Kerfeld, T. Pascher, and V. Sundstrom, "Spectroscopic properties of the carotenoid 3'-hydroxyechinenone in the orange carotenoid protein from the cyanobacterium arthrospira maxima," *Biochemistry*, vol. 44, no. 10, pp. 3994–4003, Mar. 2005.

[8] I. Bunghez, M. Raduly, S. Doncea, I. Aksahin, and R. Ion, "Lycopene determination in tomatoes by different spectral techniques (UV-VIS, FTIR and HPLC)," *Dig. J. Nanomater. Biostructures*, vol. 6, no. 3, pp. 1349–1356, 2011.

[9] A. V. Ruban, P. Horton, and A. J. Young, "Aggregation of higher plant xanthophylls: Differences in absorption spectra and in the dependency on solvent polarity," *J. Photochem. Photobiol. B Biol.*, vol. 21, no. 2–3, pp. 229–234, Dec. 1993.

[10] A. R. Wellburn, "The spectral determination of chlorophyll-a and chlorophyll-b, as well as total carotenoids, using various solvents with spectrophotometers of different resolution," *J. Plant Physiol.*, vol. 144, no. 3, pp. 307–313, 1994.

[11] S. Shafer, "Using color to separate reflection components," *Color Res. Appl.*, vol. 10, no. 4, pp. 210–218, 1985.

[12] A. G. Mignani, L. Ciaccheri, and H. Ottevaere, "Visible and near-infrared absorption spectroscopy by an integrating sphere and optical fibers for quantifying and discriminating the adulteration of extra virgin olive oil from Tuscany," *Anal. Bioanal. Chem.*, vol. 399, no. 3, pp. 1315–1324, 2011.

[13] N. Nelson and B. Prezelin, "Calibration of an integrating sphere for determining the absorption-coefficient of scattering suspensions," *Appl. Opt.*, vol. 32, no. 33, pp. 6710–6717, Nov. 1993.

[14] A.R. Alfano, *The Supercontinuum Laser Source*, 2nd ed. Berlin, Germany: Springer, 2006.

[15] C. F. Kaminski, R. S. Watt, A. D. Elder, J. H. Frank, and J. Hult, "Supercontinuum radiation for applications in chemical sensing and microscopy," *Appl. Phys. B*, vol. 92, no. 3, pp. 367–378, Aug. 2008.

[16] J. Stover, *Optical Scattering: Measurement and Analysis*, 1st ed. Bellingham, WA, USA: SPIE Optical Engineering Press, 1995.

[17] V. Vanderbilt, L. Grant, L. Biehl, and B. Robinson, "Specular, diffuse, and polarized light scattered by 2 wheat canopies," *Appl. Opt.*, vol. 24, no. 15, pp. 2408–2418, 1985.

[18] I. Kralj Cigić and H. Prosen, "An overview of conventional and emerging analytical methods for the determination of mycotoxins," *Int. J. Mol. Sci.*, vol. 10, no. 1, pp. 62–115, Jan. 2009.

[19] A. G. Griesbeck, J. Neudörfl, and A. de Kiff, "Photoinduced electron-transfer chemistry of the bielectrophoric N-phthaloyl derivatives of the amino acids tyrosine, histidine and tryptophan," *Beilstein J. Org. Chem.*, vol. 7, pp. 518–524, Apr. 2011.

[20] B. Osborne, T. Fearn, and P. Hindle, *Practical NIR Spectroscopy with Applications in Food and Beverage Analysis*. London, UK: Longman Scientific and Technical, 1993.

[21] R. McCluney, *Radiometry and Photometry*. Boston, MA, USA: Artech House Inc., 1994.

[22] S. Van Overmeire, H. Ottevaere, G. Desmet, and H. Thienpont, "Miniaturized detection system for fluorescence and absorbance measurements in chromatographic applications," *IEEE J. Sel. Top. Quantum Electron.*, vol. 14, no. 1, pp. 140–150, Jan. 2008.

[23] T. Verschooten, M. Callewaert, M. Ciaccheri, M. Vervaeke, J. Van Erps, M. Vervaeke, A. Mignani, H. Thienpont, and H. Ottevaere, "Optofluidic multi-measurement system for the online monitoring of lubricant oil," *Meas. Sci. Technol.*, Jan. 2016.

Wendy Meulebroeck (wmeulebr@vub.ac.be) is a professor and post-doctoral researcher of engineering of the Vrije Universiteit Brussel (VUB), Belgium. She is coordinating and working on multiple research and industrial projects focusing on the experimental characterization of different types of materials including ancient glasses, biological products, plastics and photosensitive polymers. She graduated as an Electrotechnical Engineer with a major in Photonics in 1998 and received her Ph.D. degree in Applied Sciences in 2004, both at the VUB.

Hugo Thienpont coordinates the Brussels Photonics Team of the Vrije Universiteit Brussel, Belgium, a group of 60 researchers who focus on photonics research and innovation. He coordinates large European networking projects and manages photonics industry projects. Since 2004, he has been General Chair of the SPIE Photonics Europe Conference. He authored more than 800 Web of Science cited publications. Since 2012, he has been Vice-Rector for Innovation and Industrial Policy.

Heidi Ottevaere graduated from the Vrije Universiteit Brussel (VUB), Belgium in 1997 as an electrotechnical engineer with a major in Photonics and received her Ph.D. degree in Applied Sciences in 2003 from the same university. She is coordinating and working on multiple research and industrial projects focusing on the design, fabrication and characterization of different types of photonic components and systems in the field of biophotonics, interferometry, holography and imaging. Since 2009, she has been a full professor of engineering of the VUB.